Fabrication of long-range ordered aluminum oxide and Fe/Au multilayered nanowires for 3D magnetic memory

Joseph Um[1], Mohammad Reza Zamani Kouhpanji[1], Samuel Liu[1], Zohreh Nemati Porshokouh[1], Sang-Yeob Sung[1], Jürgen Kosel[2], and Bethanie Stadler[1]

[1]Department of Electrical and Computer Engineering, University of Minnesota, Minneapolis, MN 55455, USA

[2]Computer, Electrical and Mathematical Science and Engineering Division, King Abdullah University of Science and Technology, Thuwal 23955, Saudi Arabia

Large-scale long-range ordered anodic aluminum oxide and multilayered nanowires (NWs) are attractive to 3-D nanostructured material applications, such as high-density 3-D magnetic memory. This article demonstrates long-range ordered aluminum oxide made by simple and inexpensive double imprinting with line-patterned stamp and uniform iron-gold multilayered NWs fabricated by galvanostatic electrochemical deposition with a single electrolyte bath. These two structural features show potential for future high-density recording systems that require long-range ordered devices separated from each other by insulation to eliminate cross-talk.

I. INTRODUCTION

The rapid development of data storage technology has enabled memory density in magnetic hard disk drives (HDDs) and solid-state devices to reach 1 Tbit/in^2 with the limit of 2-D arrays in sight. For example, the limit for heat-assisted magnetic recording-based HDDs is 10 Tbit/in^2 [1]. A further increase in the memory density is possible with 3-D approaches [1], [2], such as Fe/Au multilayered magnetic nanowires (NWs) in which the bits are stored in Fe layers.

Compared to 3-D flash memory which experiences oxide crystal lattice damage by quantum tunneling and hot electron injection, leading to a finite lifespan, the NW-based 3-D memory (e.g., racetrack memory) does not experience a wear-out phenomenon because it uses electron spins and magnetic moments for read and write, which give it a fundamental advantage of high reliability. To realize NW-based 3-D memory, two structural features are required, long-range ordered anodic aluminum oxide (AAO) templates and multilayered NWs. We explored these features simultaneously via custom and commercial templates.

First, porous AAO templates are frequently used as templates to grow NWs by electrochemical deposition. The pores of AAO, however, have only short-range order as naturally formed during conventional two-step anodization of aluminum (Al), usually in the range of 20 times the interpore

distance [3]. It is desirable to make long-range ordered AAO so that NW devices can be grown densely at known locations and contacted easily for applications, such as HDD read sensors [4], bit patterned media, and magnetic random-access memory (MRAM)/spin-transfer torque (STT)-MRAM.

Long-range ordered AAO is possible with imprinting methods in which stamps with hexagonally ordered arrays of nanostructures such as nanopyramids [3], nanoconvexes [5], and nanopillars [4], [6]–[8] are pressed into Al foils or Al films, and the resulting imprints guide pore growth during subsequent anodization. These stamps were made by conventional photolithography that requires many steps and e-beam lithography that is expensive and slow for millimeter square scale area [9]. Stamps with simple line patterns, instead of hexagonally arranged dots, take far less time to fabricate since the time for patterning is proportional to the number of structures [10]. Also, inexpensive Si stamps with line patterns at nanometer scales are commercially available.

The second feature of interest is multilayered NWs. Here, we use a single electrolyte bath for Fe and Au which, compared to transferring between two different baths, lowers the risk of contamination, such as corrosion at the interface between Fe and Au layers. Also, high-density vertical memory will require many Fe layers, which would be difficult with two separate baths.

There has been research on multilayered NWs for different materials deposited with single baths [11]–[21], mostly using AAO templates with pore diameters larger than 100 nm. The pore diameter of AAO decreases as the pore density (number of pores /cm^2) increases, for example, AAO with 40-, 100-, and 200-nm pore diameters have densities of about 10^{10}, 10^9, and 10^8/cm^2, respectively. To increase the number of NWs, in other words to increase the memory density, AAO with small pore diameters should be used. Using small pore templates for growing NWs requires much attention compared to larger pores since any hydrogen gas bubbles, which can accompany electrodeposition, may be trapped in small pores, hindering the deposition.

In this article, we introduce long-range ordered AAO made by double imprinting method with the line-patterned stamp and Fe/Au multilayered NWs using commercial AAO with 40-nm pore diameter and a single electrolyte bath, which could be useful for fabrication of 3-D magnetic memory in the near future. The line stamps, the long-range ordered AAO, and the Fe/Au NWs were characterized using scanning electron microscopy (SEM, JEOL 6500) and transmission electron microscopy (TEM, FEI Tecnai T12). The magnetic properties of Fe/Au NWs were measured using vibrating sample magnetometry (VSM, LakeShore 7410).

II. EXPERIMENTAL

A. Long-Range Ordered AAO

In this article, Si masters were purchased from LightSmyth Technologies that were 12.5 mm X 12.5 mm in total size and had line patterns of 139-nm protruded linewidth and a period of 278 nm. These masters were cleaned with acetone, isopropyl alcohol, and deionized (DI) water. A 200-nm Ni film was

evaporated onto these Si masters as a seed layer, and then more Ni was electrochemically deposited to produce a Ni stamp that contained complementary line patterns. The electrodeposited Ni film (= Ni stamp) was delaminated from the Si master when it became thick (~ 145 ± 12 µm) due to film stress, and the original Si master can be reused to make many Ni stamps. Next, Al foils (99.999%) from Alfa Aesar were degreased in acetone for 10 min, rinsed with DI water, and soaked in 1 M NaOH for 3 min to remove the natural Al oxide. The Ni stamps were imprinted into Al foils using a hydraulic press with 1200-1500 kg/cm^2, rotated 60˚, and imprinted again to make double imprinted areas from which the nanopores were grown during anodization at 160 V with 1 wt% H_3PO_4 at 0 ˚C, as shown in Fig. 1. The oxide growth rate by anodization was 1.14 µm/h.

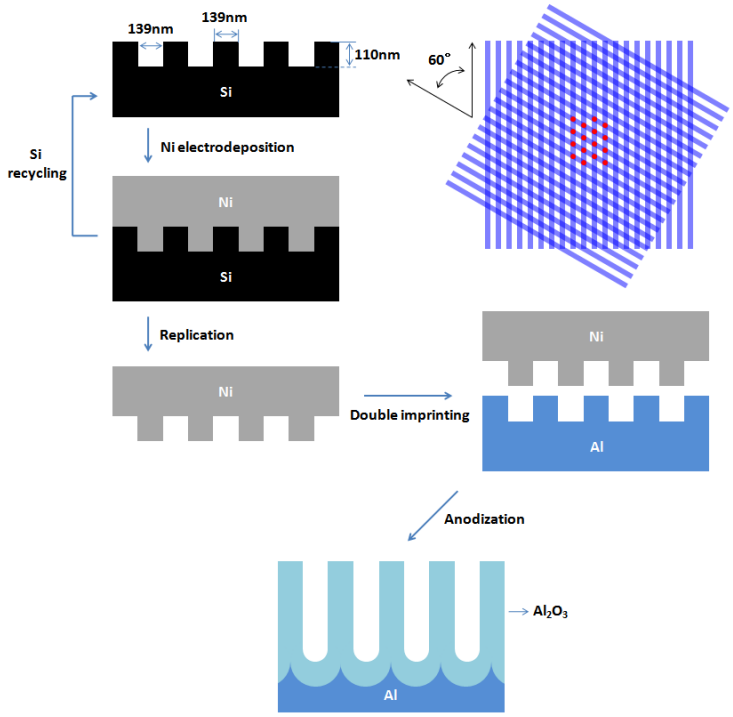

Fig. 1. Schematic of double imprinting method.

B. Fe/Au Multilayered Nanowires

Simultaneously with the synthesis of the above ordered AAO arrays, Fe/Au NWs were fabricated using commercial AAO with 40-nm pore diameter purchased from InRedox. The Fe/Au single electrolyte bath was a mixture of iron sulfate (source of Fe^{2+}), potassium dicyanoaurate (source of Au^{+}), boric acid (pH buffer), ammonium chloride (to increase the conductivity of the solution and to inhibit pH increase on a working electrode surface) [22], [23], saccharin sodium (to make grains smooth and regular) [24], malonic acid (complexing agent for Fe^{3+} ions) [24], ascorbic acid (to prevent Fe^{2+} from becoming Fe^{3+} by oxidation) [24], and sodium dodecyl sulfate (to enhance the wetting and to remove hydrogen gas bubbles in pores of AAO) [24]. The molar ratio of Fe and Au was 40:1. The pH of the solution was in the

range of 2.5-3. Prior to electrodeposition, a 7-nm Ti film was sputtered on the one side of AAO as an adhesion layer between AAO and subsequently a 500-nm Cu film, which was an electrical contact for electrodeposition. In electrodeposition, AAO was used as a working electrode, and a platinum mesh was used as a counter electrode. The electrolyte bath was stirred vigorously at 300 rpm during electrodeposition. A 2-μm Cu seed layer was first electrodeposited in AAO using a bath consisting of copper sulfate and boric acid at -0.25 V versus a Ag/AgCl reference electrode at room temperature. After sonicating and rinsing the AAO in DI water, Fe/Au layers were electrodeposited in the AAO at room temperature with two different current pulses: the current densities below -10 mA/cm^2 and above -2 mA/cm^2 for Fe and Au, respectively [12]. The durations for both Fe and Au pulses were adjusted to control the length of both Fe and Au segments, for example, the pulse times for Fe (10 nm)/Au (6 nm) NWs were 0.7 and 3 s, respectively. A rest pulse of 1 s also was used after Fe and Au pulses in order to maintain a constant concentration of metal ions of electrolyte in AAO pores for uniform growth of NWs [25]. The whole deposition time is simply the number of bilayers multiplied by the sum of the pulse time and the rest pulse time, e.g., deposition time for 400-bilayered Fe (10 nm)/Au (6 nm) = 400 × (Fe 0.7 s + Rest 1 s + Au 3 s + Rest 1 s) = 2280 s.

For SEM measurements, AAO with Fe/Au multilayered NWs was cleaved at the center, and a cross section of the template was coated with a 5-nm carbon film. For TEM measurements, AAO was dissolved in 1 M NaOH to free the NWs from the AAO, followed by DI water rinse.

III. RESULTS AND DISCUSSION

A. Long-Range Ordered AAO

In this section, cost-effective long-range order is achieved by two means. First, line patterns are used rather than dot patterns, and second, the e-beam pattern is used to produce not Si stamps but Si masters, from which many Ni stamps are made. Fig. 2(a) shows the line pattern on a Ni stamp replicated by Ni electrodeposition on a Si master, and the inset shows the whole Ni stamp. The stamp looks blue since the line period demonstrated here is 278 nm, and blue light with a wavelength of 278 nm is diffracted off the Ni stamp at 0˚ and 180˚. The linewidth is about 160 nm, and the sidewalls of the lines are slightly sloped. This gives the Ni lines a periodic trapezoidal cross section which enables successful nanoimprinting.

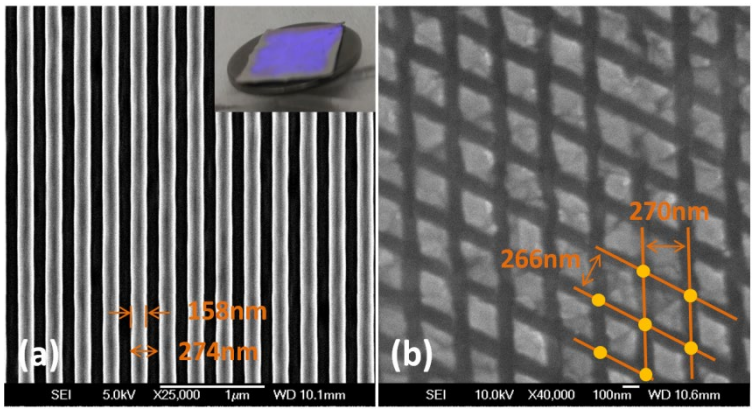

Fig. 2. SEM images of (a) line pattern on Ni stamp with inset showing the Ni stamp and (b) double imprinted Al precursor.

When the Al precursor is double imprinted, the resulting pattern is shown in Fig. 2(b). The double imprinted area is marked with orange dots, which are hexagonally arranged. These sunken features will guide the pore growth during anodization because they provide low energy sites for pores to start [10]. The distance between orange dots is similar to the line period of the Ni stamp and the Si master. Simply, the relationship between interpore distance (D_{int}) and line spacing is $D_{\text{int}} = \frac{\text{Line spacing}}{\frac{\sqrt{3}}{2}}$.

For this imprinted Al precursor, the calculated interpore distance is about 300-320 nm based on the line spacing shown in Fig. 2(b). The proper anodization voltage (V) required to match the interpore distance (D_{int}) is calculated by $D_{\text{int}} = \alpha \times V$, where α is a correlation parameter and ranges from 2 to 2.8 [3], [10], [26]. Anodization of the imprinted Al precursor at 160 V for 1 h resulted in AAO with long-range ordered pores shown in Fig. 3. The interpore distances were in the range of 295-315 nm, which is quite similar to the calculated values. The inset of Fig. 3 shows AAO with a patterned region that has ordered pores (blue area with 1 cm diameter) surrounded by the not-imprinted region that has natural short-range ordered pores (gray area). The average pore diameter measured by ImageJ was 56 ± 7 nm. In addition, denser NW devices can be made if a similar process is used with smaller line period stamps and anodization voltages.

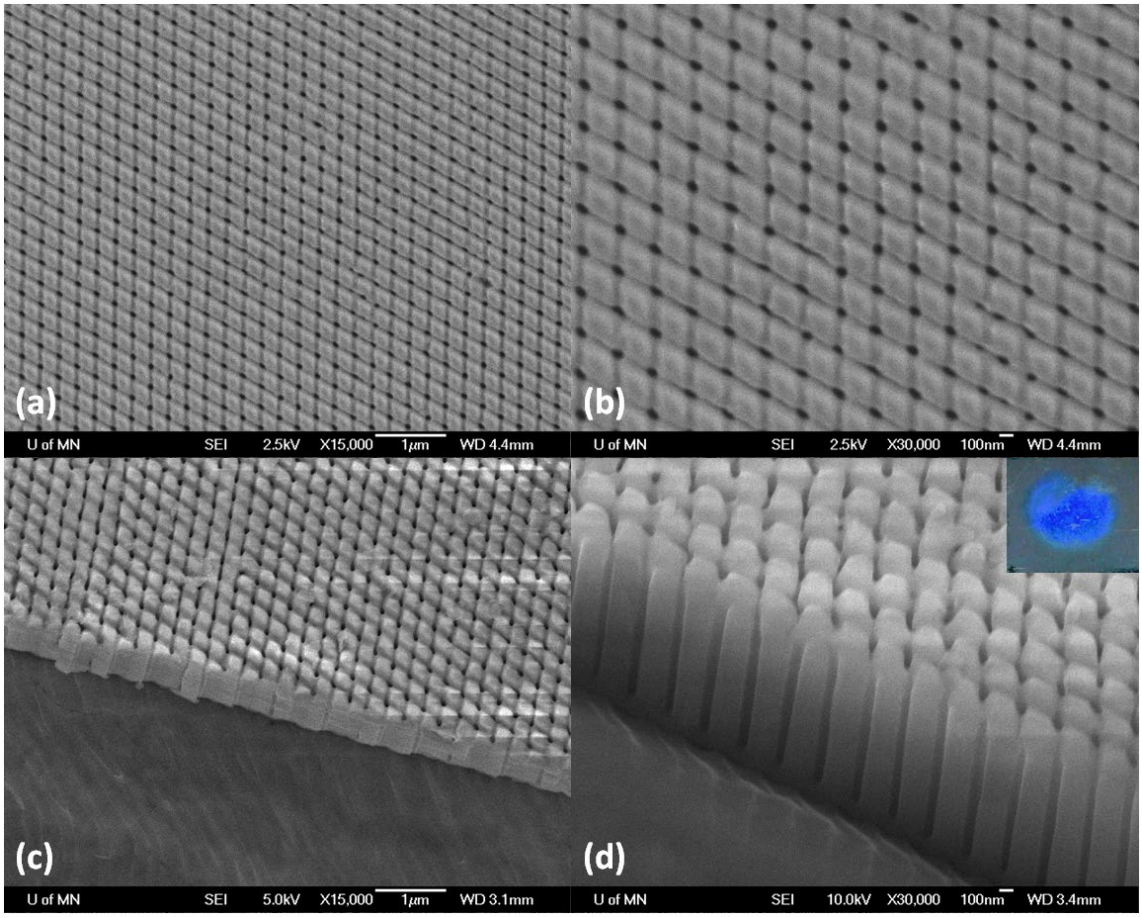

Fig. 3. (a, b, c, d) AAO by anodization of double imprinted Al at different magnifications with inset showing ordered and random regions. Inset: the ordered pores diffract blue light.

B. Fe/Au Multilayered Nanowires

As mentioned above, a 2-μm Cu seed layer was first deposited in AAO in order to block the pores to avoid electrolyte leakage, to fill dendrite structures that often form at the bottom of the AAO pores, and to provide nucleation sites for simultaneous NW growth [15], [27]. Growing NWs without the Cu seed layer can cause nonuniform NW lengths, especially nonuniform segment lengths for multilayered NWs.

Constant current densities and time durations were used throughout the whole deposition process so that the deposited charges were fixed for Fe and Au segments. This galvanostatic method ensures that the lengths of both Fe and Au segments are constant along the entire length of the NWs, especially compared to potentiostatic methods [28], [29], unless the pore size of AAO has a distinctive variation or hydrogen bubbles block pores. In this way, 400 bilayers were made with high uniformity.

Segment lengths were confirmed with SEM. Typical SEM analysis usually involves either images of small areas (at most about ten NWs in one SEM image) or energy-dispersive X-ray spectroscopy to check compositions of single NWs or the surface of a filled AAO cross section. Here, we show that SEM images with backscattered electrons provide excellent contrast for segments, even well into the array (up to 2 μm depth from AAO cross section surface), as shown in Fig. 4. TEM images of the NWs are also shown in Fig. 5.

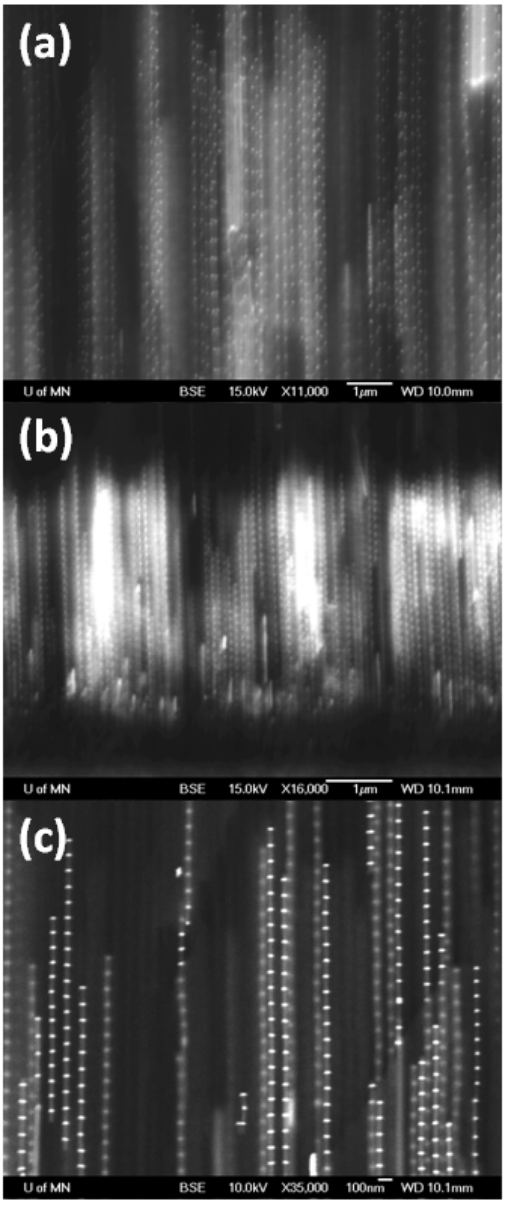

Fig. 4. SEM backscattered electron images of AAO cross section showing Fe (gray)/Au (white) multilayered NWs in the array. (a) Fe (300 nm)/Au (50 nm) NWs. (b) Fe (50 nm)/Au (60 nm) NWs. (c) Fe (100 nm)/Au (20 nm) NWs.

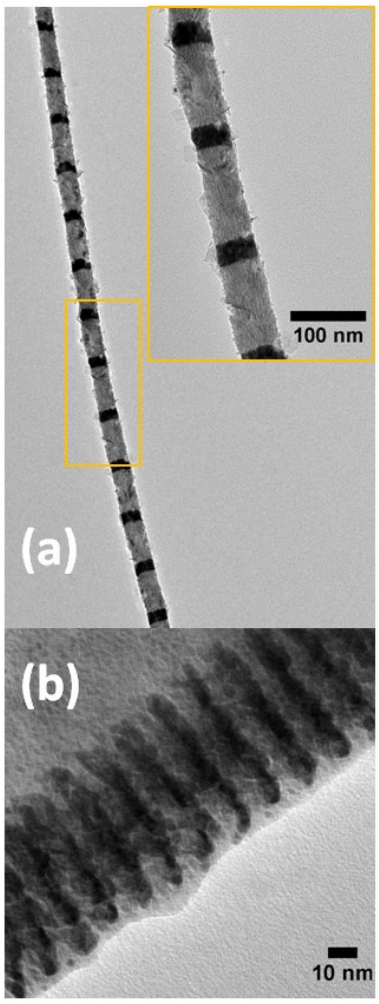

Fig. 5. TEM images of Fe (gray)/Au (black) multilayered NWs. (a) Fe (120 nm)/Au (30 nm) NW. (b) Fe (10 nm)/Au (6 nm) NW.

As shown in Figs. 4 and 5, the segment lengths of all different types of Fe/Au NWs are uniform. The length of both Fe and Au segments of NWs can be simply controlled by changing the pulse duration, thereby adjusting the amount of deposited charges. Lee *et al.* [12] investigated Fe and Au composition ratio depending on the current density in electrodeposition, indicating that an alloy was not formed by using the current densities below -10 mA/cm^2 for Fe and above -2 mA/cm^2 for Au.

The magnetic hysteresis loops of an array of 40-nm diameter Fe (120 nm)/Au (30 nm) NWs in AAO were measured at room temperature by VSM as shown in Fig. 6. The coercivities with the field applied parallel and perpendicular to NW long axis were measured as 137.2 and 76.3 Oe, respectively. The shape anisotropy field (H_d) of the Fe segments is clear based on the difference in switching field when the NWs were aligned parallel and perpendicular to the applied field. For isolated NWs, this shape anisotropy field should equal the switching field of NWs with perpendicular alignment (H_{sw} in Fig. 6),

and should also equal $2\pi M_s$, where M_s is saturation magnetization (e.g., M_s of Fe = 1707 emu/cm^3). However, when the NWs are in arrays in AAO, this value must be corrected by (1-3*P*), where *P* is the porosity of the template (e.g., *P* of AAO with 40-nm pore diameter = 12 %), meaning that $H_d = H_{sw} = 2\pi M_s(1-3P)$, or 6.9 kOe [30], [31]. This value agrees very well with the switching field shown in Fig. 6, which is a clear indication that the Fe has not oxidized and is not contaminated by the electrolyte. A single bath deposition ensured high-quality Fe segments. Although these NWs are inside an oxide template, aluminum is much lower on the Ellingham diagram than Fe, and therefore, Fe is unlikely to be oxidized while inside this well-insulating template, making these structures ideal for MRAM and STT-MRAM.

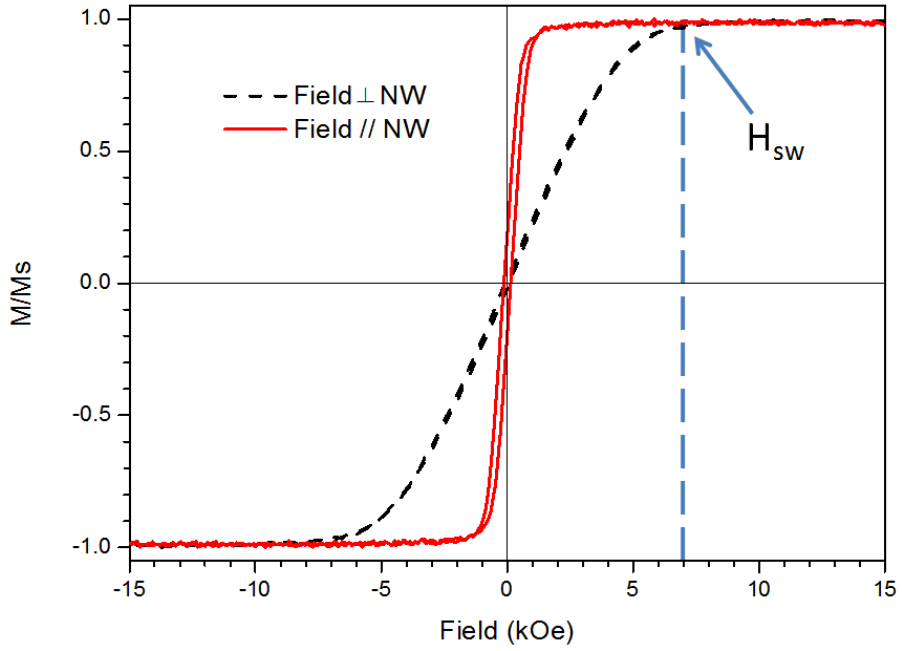

Fig. 6. Hysteresis loops of 40-nm diameter Fe (120 nm)/Au (30 nm) NWs aligned parallel and perpendicular to the magnetic field applied.

In the NW-based 3-D memory, nonmagnetic layers (e.g., Au) should be thick enough to hinder dipole interactions between magnetic layers (e.g., Fe) to avoid distortion in the stored data. The optimal lengths of Fe and Au segments will be studied in the future. Previously, we investigated the impact of length ratio for FeGa alloy and Cu segments with reduced dipole interactions between FeGa segments in order for FeGa/Cu multilayered NWs to have a high magnetostriction for sensors and actuators [15], [16].

In addition, Fe/Au NWs shown in Fig. 5(b) have 400 bilayers of Fe and Au, meaning that these NWs provide 26 Tbit/in^2 if these NWs are used for memory devices since a pore density of commercial AAO with 40-nm pore diameter is 10^{10}/cm^2 (~ 6.5 × 10^{10}/in^2). The density would be higher if more stacks are made during electrodeposition, which is just a matter of time. Moreover, if two structural features

introduced here are used together, and stamps with smaller line periods are used in double imprinting, the memory density can be even much higher.

IV. CONCLUSIONS

The large-scale long-range ordered AAO and Fe/Au multilayered NWs presented here are interesting for many 3-D nanostructured material applications. Double imprinting could be the simplest and most cost-effective method to produce long-range ordered AAO. Many types of uniform Fe/Au multilayered NWs were fabricated simply by a Cu seed layer, galvanostatic control, and deposition time for Fe and Au layers within the single electrolyte bath. This method provides a rapid and facile technique for multiple layers and lowers the risk of contamination. Also, through backscattered electron SEM, the uniformity of single NWs and NW arrays could be checked even up to 2 μm into the sample. These two techniques show potential for future high-density recording systems, such as 3-D magnetic memory, which require long-range ordered devices inside insulation to suppress crosstalk.

ACKNOWLEDGMENT

This work was supported by the National Science Foundation through the National Nano Coordinated Infrastructure Network under Award ECCS-1542202, and through the Materials Research Science and Engineering Centers Program, which was performed in the Minnesota Nano Center and the Characterization Facility, University of Minnesota, respectively.

REFERENCES

[1] Y. P. Ivanov, A. Chuvilin, S. Lopatin, and J. Kosel, "Modulated Magnetic Nanowires for Controlling Domain Wall Motion: Toward 3D Magnetic Memories," *ACS Nano*, vol. 10, no. 5, pp. 5326–5332, May 2016.

[2] S. Agramunt-Puig *et al.*, "Modeling the collective magnetic behavior of highly-packed arrays of multi-segmented nanowires," *New Journal of Physics*, vol. 18, no. 1, p. 013026, Jan. 2016.

[3] J. Choi, K. Nielsch, M. Reiche, R. B. Wehrspohn, and U. Gösele, "Fabrication of monodomain alumina pore arrays with an interpore distance smaller than the lattice constant of the imprint stamp," *Journal of Vacuum Science & Technology B: Microelectronics and Nanometer Structures*, vol. 21, no. 2, p. 763, 2003.

[4] M. M. Maqableh *et al.*, "Low-Resistivity 10 nm Diameter Magnetic Sensors," *Nano Letters*, vol. 12, no. 8, pp. 4102–4109, Jul. 2012.

[5] H. Masuda, H. Yamada, M. Satoh, H. Asoh, M. Nakao, and T. Tamamura, "Highly ordered nanochannel-array architecture in anodic alumina," *Applied Physics Letters*, vol. 71, no. 19, pp. 2770–2772, Nov. 1997.

[6] J. Zou, X. Qi, L. Tan, and B. J. H. Stadler, "Large-scale ordering of porous Si using anodic aluminum oxide grown by directed self-assembly," *Applied Physics Letters*, vol. 89, no. 9, p. 093106, Aug. 2006.

[7] P. D. McGary, L. Tan, J. Zou, B. J. H. Stadler, P. R. Downey, and A. B. Flatau, "Magnetic nanowires for acoustic sensors (invited)," *Journal of Applied Physics*, vol. 99, no. 8, p. 08B310, Apr. 2006.

[8] M. M. Maqableh *et al.*, "CPP GMR Through Nanowires," *IEEE Transactions on Magnetics*, vol. 48, no. 5, pp. 1744–1750, May 2012.
[9] B. Stadler *et al.*, "Galfenol Thin Films and Nanowires," *Sensors*, vol. 18, no. 8, p. 2643, Aug. 2018.
[10] S.-Y. Sung, M. M. Maqableh, X. Huang, K. Sai Madhukar Reddy, R. H. Victora, and B. J. H. Stadler, "Metallic 10 nm Diameter Magnetic Sensors and Large-Scale Ordered Arrays," *IEEE Transactions on Magnetics*, vol. 50, no. 11, pp. 1–5, Nov. 2014.
[11] L. Tan and B. J. H. Stadler, "Fabrication and magnetic behavior of Co/Cu multilayered nanowires," *Journal of Materials Research*, vol. 21, no. 11, pp. 2870–2875, Nov. 2006.
[12] J. H. Lee *et al.*, "Iron–Gold Barcode Nanowires," *Angewandte Chemie International Edition*, vol. 46, no. 20, pp. 3663–3667, May 2007.
[13] J. U. Cho, J.-H. Wu, J. H. Min, J. H. Lee, H.-L. Liu, and Y. K. Kim, "Effect of field deposition and pore size on Co/Cu barcode nanowires by electrodeposition," *Journal of Magnetism and Magnetic Materials*, vol. 310, no. 2, pp. 2420–2422, Mar. 2007.
[14] L. Tan, P. D. McGary, and B. J. H. Stadler, "Controlling the angular response of magnetoresistance in Co/Cu multilayered nanowires using Co crystallographic orientation," *Journal of Applied Physics*, vol. 103, no. 7, p. 07B504, Apr. 2008.
[15] K. S. M. Reddy, J. J. Park, S.-M. Na, M. M. Maqableh, A. B. Flatau, and B. J. H. Stadler, "Electrochemical Synthesis of Magnetostrictive Fe-Ga/Cu Multilayered Nanowire Arrays with Tailored Magnetic Response," *Advanced Functional Materials*, vol. 21, no. 24, pp. 4677–4683, Dec. 2011.
[16] K. S. M. Reddy, J. Jin Park, M. M. Maqableh, A. B. Flatau, and B. J. H. Stadler, "Magnetization reversal mechanisms in 35-nm diameter $Fe_{1-x}Ga_x$/Cu multilayered nanowires," *Journal of Applied Physics*, vol. 111, no. 7, p. 07A920, Apr. 2012.
[17] I. T. Jeon *et al.*, "Magnetic NiFe/Au barcode nanowires with self-powered motion," *Journal of Applied Physics*, vol. 111, no. 7, p. 07B513, Apr. 2012.
[18] B. G. Kim, S. J. Yoon, I. T. Jeon, K. H. Kim, J. H. Wu, and Y. K. Kim, "Dimensional Dependence of Magnetic Properties in Arrays of CoFe/Au Barcode Nanowire," *IEEE Transactions on Magnetics*, vol. 48, no. 11, pp. 3929–3932, Nov. 2012.
[19] J. García *et al.*, "Template-assisted Co-Ni alloys and multisegmented nanowires with tuned magnetic anisotropy: Co-Ni alloys and multisegmented NWs with tuned magnetic anisotropy," *physica status solidi (a)*, vol. 211, no. 5, pp. 1041–1047, May 2014.
[20] B. Özkale *et al.*, "Multisegmented FeCo/Cu Nanowires: Electrosynthesis, Characterization, and Magnetic Control of Biomolecule Desorption," *ACS Applied Materials & Interfaces*, vol. 7, no. 13, pp. 7389–7396, Apr. 2015.
[21] A. Serrà, G. Vázquez-Mariño, J. García-Torres, M. Bosch, and E. Vallés, "Magnetic Actuation of Multifunctional Nanorobotic Platforms to Induce Cancer Cell Death," *Advanced Biosystems*, vol. 2, no. 2, p. 1700220, Feb. 2018.
[22] C. A. Marozzi and A. C. Chialvo, "Development of electrode morphologies of interest in electrocatalysis. Part 1: Electrodeposited porous nickel electrodes," *Electrochimica Acta*, vol. 45, no. 13, pp. 2111–2120, Mar. 2000.
[23] J. Ji, W. C. Cooper, D. B. Dreisinger, and E. Peters, "Surface pH measurements during nickel electrodeposition," *Journal of Applied Electrochemistry*, vol. 25, no. 7, Jul. 1995.
[24] A. Ghemes *et al.*, "Controlled Electrodeposition and Magnetic Properties of $Co_{35}Fe_{65}$ Nanowires with High Saturation Magnetization," *Journal of The Electrochemical Society*, vol. 164, no. 2, pp. D13–D22, 2017.

[25] J. Azevedo, C. T. Sousa, A. Mendes, and J. P. Araújo, “Influence of the Rest Pulse Duration in Pulsed Electrodeposition of Fe Nanowires,” *Journal of Nanoscience and Nanotechnology*, vol. 12, no. 12, pp. 9112–9117, Dec. 2012.
[26] W. Lee, R. Ji, U. Gösele, and K. Nielsch, “Fast fabrication of long-range ordered porous alumina membranes by hard anodization,” *Nature Materials*, vol. 5, no. 9, pp. 741–747, Sep. 2006.
[27] B. Jang *et al.*, “Fabrication of Segmented Au/Co/Au Nanowires: Insights in the Quality of Co/Au Junctions,” *ACS Applied Materials & Interfaces*, vol. 6, no. 16, pp. 14583–14589, Aug. 2014.
[28] D. Shore *et al.*, “Electrodeposited Fe and Fe–Au nanowires as MRI contrast agents,” *Chemical Communications*, vol. 52, no. 85, pp. 12634–12637, 2016.
[29] D. E. Shore, T. Dileepan, J. F. Modiano, M. K. Jenkins, and B. J. H. Stadler, “Enrichment and Quantification of Epitope-specific CD4+ T Lymphocytes using Ferromagnetic Iron-gold and Nickel Nanowires,” *Scientific Reports*, vol. 8, no. 1, Dec. 2018.
[30] M. Darques, A. Encinas, L. Vila, and L. Piraux, “Controlled changes in the microstructure and magnetic anisotropy in arrays of electrodeposited Co nanowires induced by the solution pH,” *Journal of Physics D: Applied Physics*, vol. 37, no. 10, pp. 1411–1416, Apr. 2004.
[31] W. Zhou *et al.*, “Development of a Biolabeling System Using Ferromagnetic Nanowires,” *IEEE J. Electromagn. RF Microw. Med. Biol.*, vol. 3, no. 2, pp. 134–142, Jun. 2019.